

# In Situ Visualization and Quantification of Electrical Self-Heating in Conjugated Polymer Diodes Using Raman Spectroscopy

Sudeshna Maity, Charusheela Ramanan, Freck Ariese, Roderick C. I. MacKenzie, and Elizabeth von Hauff\*

Self-heating in organic electronics can lead to anomalous electrical performance and even accelerated degradation. However, in the case of disordered organic semiconductors, self-heating effects are difficult to quantify using electrical techniques alone due to complex transport properties. Therefore, more direct methods are needed to monitor the impact of self-heating on device performance. Here, self-heating in poly[2,6-(4,4-bis-(2-ethylhexyl)-4H-cyclopenta [2,1-b;3,4-b'] dithiophene)-alt-4,7(2,1,3-benzothiadiazole)] (PCPDTBT) diodes is visualized using Raman spectroscopy, and thermal effects due to self-heating are quantified by exploiting temperature-dependent shifts in the polymer vibrational modes. The temperature increases due to self-heating are quantified by correlating the Raman shifts observed in electrically biased diodes with temperature-dependent Raman measurements. Temperature elevations up to 75 K are demonstrated in the PCPDTBT diodes at moderate power of about 2.6–3.3 W cm<sup>-2</sup>. Numerical modeling rationalizes the significant role of Joule and recombination heating on the diode current–voltage characteristics. This work demonstrates a facile approach for in situ monitoring of self-heating in organic semiconductors for a range of applications, from fundamental transport studies to thermal management in devices.

## 1. Introduction

Organic semiconductors have great potential in emerging (opto-) electronic applications,<sup>[1–3]</sup> due to the enormous versatility to tune the properties via dedicated design of the chemical structure.<sup>[4–13]</sup> However, organic electronic applications are currently limited by issues related to a variety of chemical, mechanical, and morphological instabilities<sup>[14–21]</sup> of organic thin films,<sup>[22]</sup> functional layers,<sup>[23]</sup> device interfaces,<sup>[23,24]</sup> and substrates.<sup>[25,26]</sup> One important, yet often neglected, factor contributing to performance loss in organic electronics is *self-heating*, whereby electrical energy is converted to thermal energy. Self-heating may originate from three main phenomena: 1) Joule heating<sup>[27–31]</sup> occurs when electrical energy is dissipated as heat because of the flow of current, 2) recombination heating results when electrical energy that is lost during

recombination processes is absorbed by lattice phonons,<sup>[30,32,33]</sup> and 3) Peltier heating and cooling can take place due to current flow at material hetero-junctions.<sup>[34]</sup> These processes have been studied in the context of thermal management for operational inorganic devices,<sup>[34–36]</sup> but have so far received less attention in the field of organic electronics. However, the development of commercially feasible organic technologies necessitates higher current densities and more complex device architectures than are currently employed. This growing need therefore demands a detailed understanding of self-heating. Specifically, in the case of organic electronics, the low thermal conductivity ( $\approx 0.2 \text{ W m}^{-1} \text{ K}^{-1}$ ) of organic semiconductors prevents rapid heat dissipation, which can result in hot spots<sup>[37–39]</sup> and significant thermal gradients within the device. In extreme cases, heating can lead to thermal expansion,<sup>[40,41]</sup> fractures,<sup>[40,42]</sup> diffusion of interlayer materials,<sup>[43,44]</sup> delamination,<sup>[41,44]</sup> as well as morphological,<sup>[41,43,44]</sup> or even material, phase changes.<sup>[44]</sup> Self-heating has been reported to result in anomalies in the electrical properties of organic devices at high operating powers, such as the appearance of negative capacitance<sup>[45,46]</sup> and/or negative differential resistance.<sup>[47–50]</sup> There have been many reports that apply electrical techniques to study self-heating in organic devices based on small molecules.<sup>[46–54]</sup> Particular focus has been placed on studying Joule heating in organic light emitting diodes (OLED) due to the characteristically high operating current densities required for device operation.


S. Maity, C. Ramanan, F. Ariese, E. von Hauff  
Department of Physics and Astronomy  
Vrije Universiteit Amsterdam  
De Boelelaan 1081, HV, Amsterdam 1081, The Netherlands  
E-mail: e.l.von.hauff@vu.nl

C. Ramanan  
Max Planck Institute for Polymer Research  
Ackermannweg 10, 55128 Mainz, Germany

R. C. I. MacKenzie  
Department of Engineering  
Durham University  
Lower Mount Joy  
South Road, Durham DH1 3LE, UK

E. von Hauff  
Fraunhofer Institute for Organic Electronics  
Electron Beam and Plasma Technology (FEP)  
01277 Dresden, Germany

E. von Hauff  
Faculty of Electrical and Computer Engineering  
Technical University of Dresden  
01069 Dresden, Germany

 The ORCID identification number(s) for the author(s) of this article can be found under <https://doi.org/10.1002/aelm.202101208>.

© 2022 The Authors. Advanced Electronic Materials published by Wiley-VCH GmbH. This is an open access article under the terms of the Creative Commons Attribution License, which permits use, distribution and reproduction in any medium, provided the original work is properly cited.

DOI: 10.1002/aelm.202101208

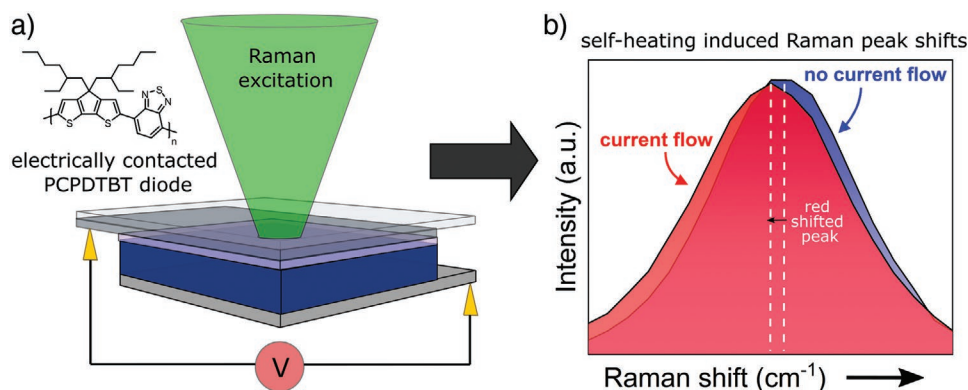


**Figure 1.** Overview of the experimental design: a) Schematic diagram of coupled Raman-applied DC voltage measurement setup and b) example of the observed shift in the Raman mode induced by self-heating. The Raman shift was observed to be between 0.1 and 1.5  $\text{cm}^{-1}$  depending on the applied bias voltage.

We are, however, unaware of any studies investigating self-heating in disordered organic semiconductors, such as conjugated polymers, despite their interesting potential in opto-electronic and electronic applications.<sup>[55]</sup> This may be because the physical mechanisms governing the electronic properties of disordered organic semiconductors are still not fully understood.<sup>[19,56–58]</sup> Therefore, it is challenging to provide a quantitative description of self-heating in polymer devices based on electrical studies alone. New, direct approaches for in situ temperature monitoring are required to assess the effect of self-heating in these devices.

Vibrational spectroscopies, i.e., infrared (IR)<sup>[27,30,59]</sup> and Raman<sup>[60–62]</sup> experiments, are promising in this respect, as they can be applied for direct, non-destructive, in situ temperature measurements on operational devices. One of the most commonly used methods to optically monitor temperature is Raman thermometry based on the temperature-induced change in the relative intensity of the Stokes and anti-Stokes lines.<sup>[60,61]</sup> However, this approach requires a highly specialized Raman setup in order to reliably detect the weak anti-Stokes lines, and the method cannot be applied to disordered materials that display no major low-wavenumber Raman modes. Further, the Stokes/Antistokes approach requires that either the height or the area of both the Stokes and Antistokes modes is evaluated, and therefore small errors in the baseline subtraction can result in large errors in the extrapolated temperatures. A related, but more straightforward, method of Raman thermometry is to monitor temperature-dependent mode softening. Increasing temperature results in lattice expansion, which correlates with an increase in the interatomic distances and a decrease in the interatomic forces. This manifests as a shift in the Raman peak position.<sup>[62–65]</sup> The shifting of Raman modes with temperature is well documented in the literature for many inorganic and organic semiconductors.<sup>[66–71]</sup> However, this approach has not yet been exploited for the in situ monitoring of self-heating in organic electronics. In contrast to inorganic semiconductors, organic semiconductors have prominent Raman modes in the fingerprint region ( $\approx 500\text{--}1800\text{ cm}^{-1}$ ) which can be monitored with standard Raman setups. We demonstrate how combining Raman spectroscopy with electrical measurements offers a straightforward, non-destructive approach to quantify self-heating in organic electronic devices under relevant operating conditions.

In this work we investigate self-heating in the donor(D)-acceptor(A) polymer poly[2,6-(4,4-bis-(2-ethylhexyl)-4H-cyclopenta [2,1-b;3,4-b'] dithiophene)-alt-4,7(2,1,3-benzothiadiazole)] (PCPDTBT) by exploiting temperature-induced shifting of the Raman modes (Figure 1) in the region 800–1600  $\text{cm}^{-1}$ . We quantify the relationship between Raman peak position and temperature with temperature-dependent measurements on PCPDTBT films, which we compare to the shifts of the Raman peaks observed in PCPDTBT diodes. We use these results to quantify the self-heating in the diodes, and use computational methods to determine the physical cause of self-heating. Numerical modeling of the current-voltage curves of the diodes reveals that recombination heating dominates at low voltages, while Joule heating dominates at higher voltages. Our work illustrates a promising and facile approach that combines Raman spectroscopy with electrical characterization for the in situ monitoring of self-heating in organic semiconductors for applications ranging from fundamental transport studies to thermal management in devices.

## 2. Results and Discussion

### 2.1. In Situ Raman Spectra Measured on PCPDTBT Diodes

The in situ Raman spectra from an ITO/PEDOT:PSS/PCPDTBT/Ca/Al diode are depicted in Figure 2. For comparison to these results, the in situ Raman spectra from the ITO/PEDOT:PSS/PCPDTBT/MoO<sub>3</sub>/Ag diode are included in Figure S1 (Supporting Information). The band diagram of the diode along with the full, unprocessed Raman spectra with the indications of major Raman modes are shown. Zoom-ins of the Raman spectra for each of the 5 prominent Raman peaks, a) 860  $\text{cm}^{-1}$ , b) 1268  $\text{cm}^{-1}$ , c) 1347  $\text{cm}^{-1}$ , d) 1422  $\text{cm}^{-1}$ , and e) 1534  $\text{cm}^{-1}$ , as a function of voltage are presented. Multiple spectra (10) were collected under identical conditions (Methods Section) as a function of applied bias. The order of the DC bias measurements was: 0, -1, 1, -2, 2, -4, 3, 4, -3, and 3.5 V to avoid potential artifacts due to increasing electrical stress (Figure S2, Supporting Information). We reference the work by Martin et al.,<sup>[72]</sup> Provencher et al.,<sup>[73]</sup> and Aziz et al.,<sup>[74]</sup> for the assignment of these modes (Table S1, Supporting Information).

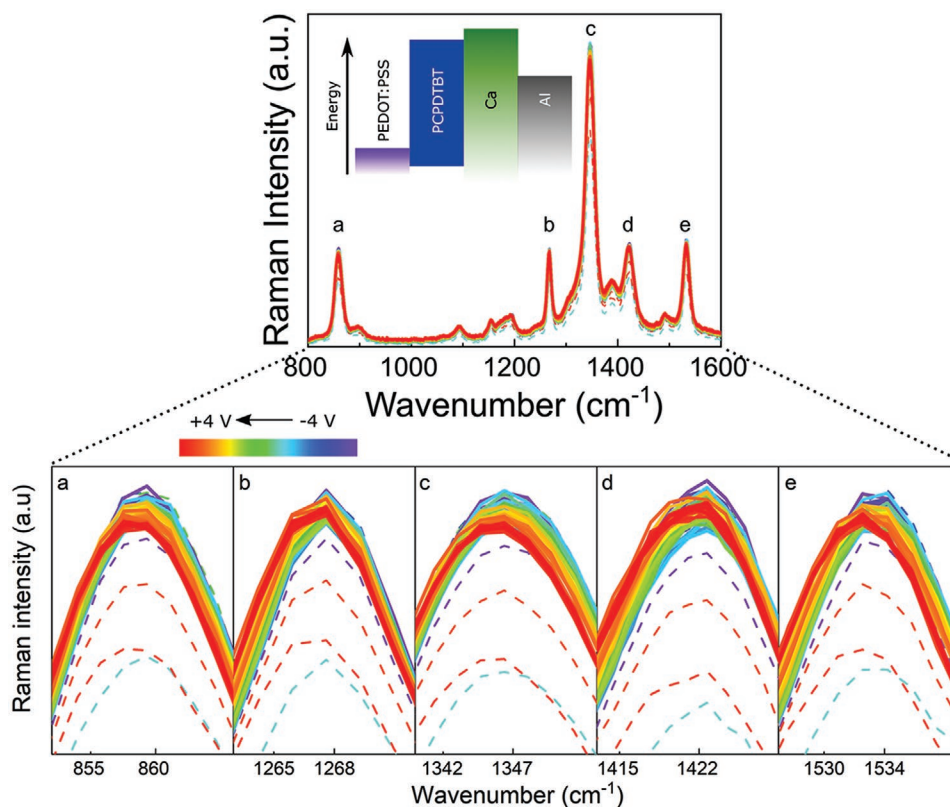


**Figure 2.** The Raman spectra of a PCPDTBT diode with Ca/Al top contacts measured while the diode was subject to applied biases between  $-4$  and  $4$  V. The inset shows the energy diagram of the diode. 10 spectra were recorded consecutively for each applied bias. The zoomed-in views of the prominent peaks at a)  $860\text{ cm}^{-1}$ , b)  $1268\text{ cm}^{-1}$ , c)  $1347\text{ cm}^{-1}$ , d)  $1422\text{ cm}^{-1}$ , and e)  $1534\text{ cm}^{-1}$  show the redshift of the peak centers with increasing positive applied bias from  $-4$  V (violet) to  $+4$  V (red), as shown in the color palette. The dashed lines indicate the first Raman spectrum in each bias series.

The color palette corresponds to an increased electrical bias, from  $-4$  V (violet) to  $+4$  V (red). Both the spectral intensity and Raman baseline were highly reproducible between all spectra across the entire measurement series (Figure S3, Supporting Information), with the exception of the first spectrum in each bias series (dashed lines in Figure 2), which consistently displayed slightly reduced intensity compared to the rest of the spectra in the series. The peak centers of all the major Raman modes shift to lower wavenumber (redshift) with increasing positive bias. The peak shifts are only observed if the diode with Ca/Al top contacts is positively biased, and no changes are observed in the spectra measured at negative bias. In contrast, the Raman spectra taken from PCPDTBT diodes with  $\text{MoO}_3/\text{Ag}$  top contacts showed that the prominent Raman modes display a redshift for both positive and negative bias (Figure S1, Supporting Information).

Figure 3 demonstrates the correlation between the current density ( $J$ ) and the shift in the position ( $\Delta X_{\text{bias}}$ ) of the major Raman modes. The  $J$  values together with the corresponding  $\Delta X_{\text{bias}}$  values are depicted as a function of applied bias ( $V$ ) for both PCPDTBT diode with the Ca/Al top contacts (Figure 3a and 3b) and for the PCPDTBT diode with the  $\text{MoO}_3/\text{Ag}$  top contacts (Figure 3c and 3d).  $\Delta X_{\text{bias}}$  is defined as the shift in the Raman peak center measured at a given bias with respect to the peak center measured at  $0$  V, i.e.,  $\Delta X_{\text{bias}} = X_{\text{bias}} - X_{0V}$ . The peak positions were extracted from a Gaussian fit (Figure S4, Supporting Information) of each peak. The average value for the peak center was determined from

the 10 spectra recorded at each bias. The error bars represent the standard deviation in the peak position values and range from  $\pm 0.01\text{ cm}^{-1}$  to  $\pm 0.06\text{ cm}^{-1}$ . Figure 3 shows that  $\Delta X_{\text{bias}}$  follows the same trend as the  $J$ - $V$  curve. The PCPDTBT diode with Ca/Al top contacts turns on at  $V = +2$  V (Figure 3a) and an exponential increase in the current density is observed for  $V > +2$  V. This is the same voltage at which  $\Delta X_{\text{bias}}$  also begins to change. There is no shift in peak position, i.e.,  $\Delta X_{\text{bias}} = 0$ , for bias values between  $-4$  and  $+2$  V where the diode exhibits negligible current density. In contrast, the  $\text{MoO}_3$  layer does not block hole transport to the Ag electrode. Consequently, the  $J$ - $V$  curve in Figure 3c is approximately symmetric around  $V = 0$  V, consistent with single-carrier diode behavior. In this case we see changes in the value of  $\Delta X_{\text{bias}}$  at applied biases above  $V = +1$  V and below  $-1$  V, corresponding to the turn-on voltages of the diode in forward and reverse bias, respectively. We note that the shift in the peak centers of the major Raman modes of PCPDTBT showed a similar, but not identical trend relative to each other with increasing applied bias.

Therefore, we conclude that changes in Raman peak position appear to be related to changes in the current density in both the diodes. This behavior may be attributed to several physical effects, including a vibrational Stark effect,<sup>[75]</sup> laser heating during the Raman measurement, and/or self-heating due to electrical operation. If the Raman mode shifts originate from a Stark effect due to the applied external voltage, we would expect no dependence on the current flow. Based on the

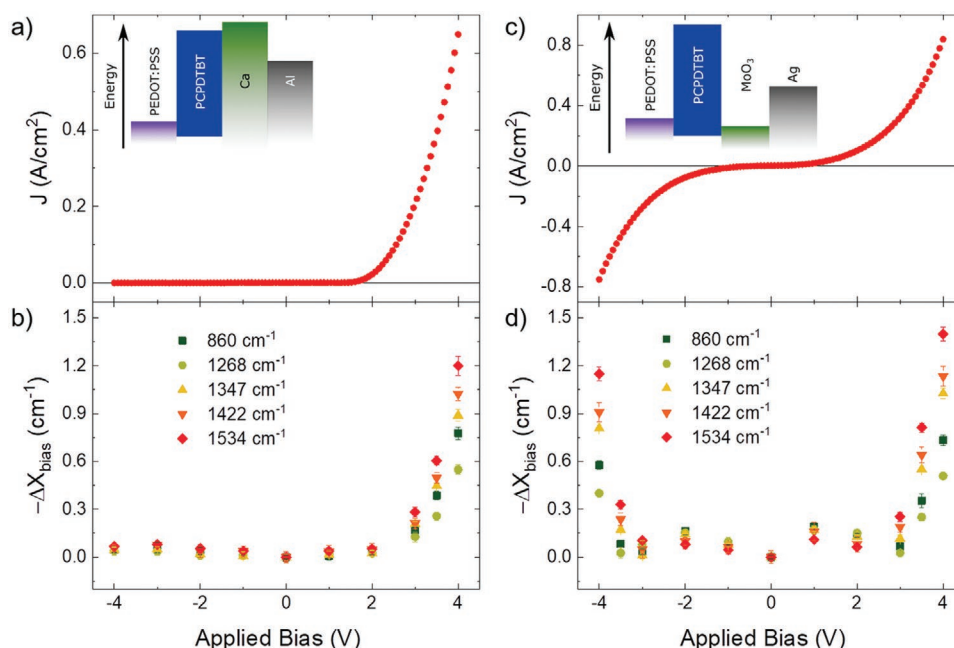


**Figure 3.** Current density ( $J$ ) and shifts in peak position ( $\Delta X_{\text{bias}}$ ) of the major Raman modes as a function of applied bias (V) measured on PCPDTBT diodes: a)  $J$ -V curve with a schematic of the diode band diagram and b)  $\Delta X_{\text{bias}}$  versus V on the PCPDTBT diode with Ca/Al top contacts, and c)  $J$ -V curve with band diagram and d)  $\Delta X_{\text{bias}}$  versus V on the PCPDTBT diode with the MoO<sub>3</sub>/Ag top contacts.

results from the diode with the Ca transport layer, we can argue strongly against this hypothesis, as we only observe peak shifts if current flows in the device. We also exclude laser heating, as the Raman spectra taken with no electrical bias are very stable over time and there are no shifts in the peak position with extended measurement time. This leaves the possibility of self-heating due to electrical operation. In order to explore the effect of electrical self-heating, we carried out temperature-dependent Raman measurements on PCPDTBT films.

## 2.2. Correlating the Shift in the Raman Modes with Temperature

Figure 4a presents the shift in Raman spectra ( $\Delta X_T$ ) of the major Raman modes measured on a PCPDTBT film as a function of temperature ( $T$ ), over a range from 298 K (room temperature) to 373 K, with steps of 10 K. The values for  $\Delta X_T$ ,

where  $\Delta X_T = X_{\text{heating}} - X_{298\text{ K}}$ , were extracted using the same protocol (Method section) as the values for  $\Delta X_{\text{bias}}$  (Figure 3). Analogous to the results in Figure 3, we note that the peak centers of the major Raman modes of PCPDTBT showed a similar, but not identical trend with temperature. While all the peak centers appear to shift linearly with temperature, the slope of peak position versus  $T$  differs between the modes. We also observe that the shift in the peak position is larger for the higher energy modes, and decreases for lower energy mode in both the electrical and temperature dependent measurement (Figure 4). The maximum shift is about 0.1% of the mode frequency for each of the peaks with an exception of 0.04% for the peak at 1268 cm<sup>-1</sup>. The full temperature dependent Raman spectra are provided in Figure S5 (Supporting Information). The spectra were recorded during both the heating and cooling cycles, and we observed good agreement between the values at each temperature during both heating and cooling procedures,

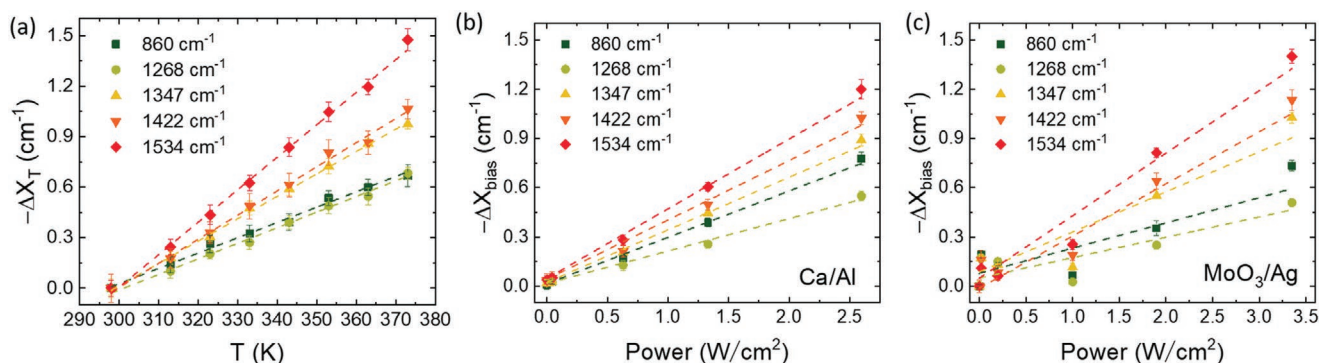


**Figure 4.** a) The shift in position ( $\Delta X_T$ ) of Raman modes as a function of temperature ( $T$ ) measured on a PCPDTBT film.  $\Delta X_{\text{bias}}$  as a function of electrical power ( $P$ ) for the diode with b) Ca/Al top contacts and c) MoO<sub>3</sub>/Ag top contacts. Dashed lines represent linear fits to each data set.

with negligible hysteresis (Figure S6, Supporting Information). Therefore, we conclude that no change in polymer morphology or structure occurred during temperature dependent measurement, and that the mode shifts are only due to heating. We further note that 373 K is well below the glass transition temperature (447 K) of PCPDTBT.<sup>[76]</sup>

We used this data to estimate the temperature induced by self-heating in the PCPDTBT diodes. We assume that the loss in electrical power correlates directly to the gain in thermal energy in order to estimate the temperature increase ( $\Delta T$ ) in the PCPDTBT layer as a function of electrical power for each applied voltage. Specifically, we compared the  $\Delta X_T$  versus  $T$  plot (Figure 4a) and the  $\Delta X_{\text{bias}}$  versus Power ( $P$ ) plots (Figure 4b,c) in order to extrapolate the temperature increase due to self-heating in the operational PCPDTBT diodes. The fitting value details are tabulated in Table S2 (Supporting Information). Based on this analysis, we find that the PCPDTBT diode with Ca/Al top contacts exhibits a  $\Delta T$  up to 75 K at  $P = 2.6 \text{ W cm}^{-2}$  (corresponding to 4 V and  $644 \text{ mA cm}^{-2}$ ), while the diode with  $\text{MoO}_3/\text{Ag}$  top contacts exhibits a  $\Delta T$  up to 72 K at  $P = 3.3 \text{ W cm}^{-2}$  (corresponding to 4 V and  $800 \text{ mA cm}^{-2}$ ). The extrapolated  $\Delta T$  values for all the major Raman modes for both the diodes are summarized in Table S3 (Supporting Information).

Our results from PCPDTBT diodes demonstrate that  $\Delta T$  up to 75 K can be reached in polymer diodes at  $P$  between  $2.6\text{--}3.3 \text{ W cm}^{-2}$ . This is consistent with results from the literature quantifying self-heating in organic electronics using analogous approaches. For example, a study on  $\text{C}_{60}$  based diodes using IR imaging combined with numerical simulation demonstrated a  $\Delta T$  of 190 K at a power of  $0.94 \text{ W}$ .<sup>[51]</sup> Other studies using IR imaging on small molecule based OLEDs reported similar increases in temperature at comparable operating powers.<sup>[27,59]</sup> A further study combined electrical measurements and modeling on small molecule-based OLED, and demonstrated  $\Delta T$  of 145 K at very high power of  $18 \text{ kW cm}^{-2}$ .<sup>[53]</sup> Fischer et al., developed an electro-thermal model to account for self-heating in the electrical characteristics of OLEDs, and demonstrated that a negative differential resistance due to self-heating results in S-shapes in the  $J$ - $V$  characteristics at  $P = 2.7 \text{ W cm}^{-2}$  corresponding to  $\Delta T = 83.6 \text{ K}$ , followed by rapid degradation.<sup>[47]</sup> We note that measurement techniques, device architectures, as well as consideration of thermal gradients and thermal hotspots versus bulk measurements can lead to discrepancies between results.

### 2.3. Modeling the Impact of Self-Heating on the PCPDTBT Diode $J$ - $V$ Characteristics

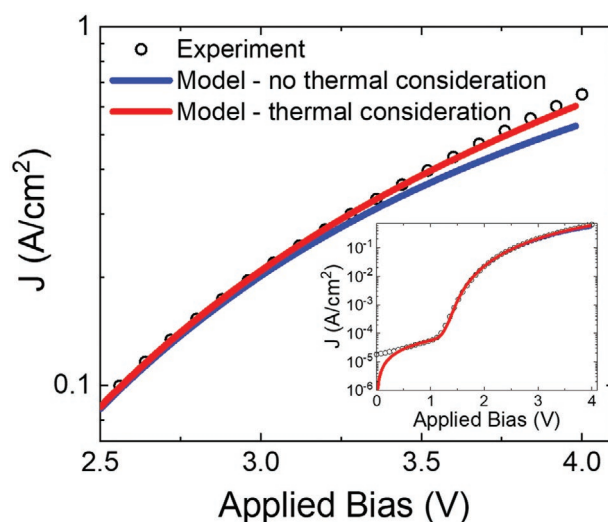
To understand the specific mechanisms leading to self-heating in PCPDTBT, we modeled the electrical properties of the diodes using the general purpose photovoltaic device model.<sup>[77–80]</sup> The model solves Poisson's equation to account for the electrostatic potential within the device, the carrier continuity equations to account for carrier conservation, and the bi-polar drift-diffusion equations to account for carrier transport due to electrical potential and thermal gradients. It also explicitly solves the Shockley-Read-Hall (SRH) equations to account for capture/recombination from trap states. The model describes

both free and trapped carriers in terms of Fermi-Dirac statistics. All equations are solved within one Jacobian to ensure numerical stability and speed. For this work we adapted the model to also solve the heat equation as a function of position, with heating terms accounting for Joule, recombination, and shunt resistance heating, as well as Peltier cooling.<sup>[81,82]</sup> All transport and heat generation equations are self-consistently derived from the Boltzmann transport equation. This enables us to describe both the electrical and thermal properties of the device, and to quantify heat generation as well as the thermal profile inside the active layer. The modeling is further detailed in the Supporting Information.

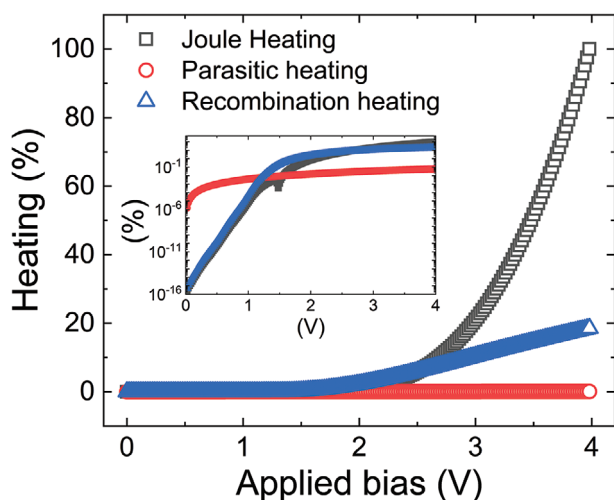
Figure 5 shows the fit of the numerical model to the experimental  $J$ - $V$  curve (symbols) from the PCPDTBT diode with Ca/Al top contacts with self-heating (red line) resulting in a thermal gradient in the active layer, and without self-heating (blue line) corresponding to a constant temperature of 298 K. The modeling results show that self-heating significantly impacts the  $J$ - $V$  curve at higher voltages (specifically, above 3 V), resulting in an increase in the current density.

Figure 6 plots the heat generated by Joule (black symbols), and recombination (blue symbols) heating within the diode as a function of voltage. We also considered parasitic heating (red symbols) to account for energy dissipated by the shunt resistance. We observe that recombination heating dominates at low to intermediate voltages (between 1 and 2.5 V). At higher voltages ( $>2.5 \text{ V}$ ), i.e., above the turn-on voltage of the diode, Joule heating is dominant. Therefore, we identify Joule heating as the principal factor responsible for the shift in the Raman modes observed at higher voltages. We note the slight dip in Joule heating at 1.5 V (inset in Figure 6) which corresponds to the built-in voltage. At this point, the energetic bands are flat and therefore Joule heating is at a minimum.

Figure 7 plots the measured/simulated temperature ( $T_{\text{extrapolated}}$ ) within the device versus dissipated electrical power ( $P$ ). The symbols represent the temperatures extracted from the shift in



**Figure 5.** The comparison between experimental  $J$ - $V$  (black symbols), numerical fit of the  $J$ - $V$  with thermal model off (blue line) and with thermal model on (red line). Inset: the full range of the applied bias considered for the simulation.



**Figure 6.** Contributions of self-heating in the PCPDTBT diodes: Joule heating (black symbols), parasitic shunt heating (red symbols), and recombination heating (blue symbols). Inset: the same data plotted on a semi-log scale to show the differences at lower bias voltages.

the major Raman modes in the PCPDTBT diode with Ca/Al (filled symbols) and MoO<sub>3</sub>/Ag (unfilled symbols) top contacts, respectively. The solid black line depicts the results from the model. The comparison indicates good agreement between the extrapolated temperature ( $T_{\text{extrapolated}}$ ) values for the different modes, as well as between the values from the experiment and from the model. The linear increase in temperature with the increase in electrical power is consistent with previous reports.<sup>[44,59]</sup>

### 3. Summary

Our results demonstrate that Raman spectroscopy can be applied as a non-destructive, in situ approach to monitor

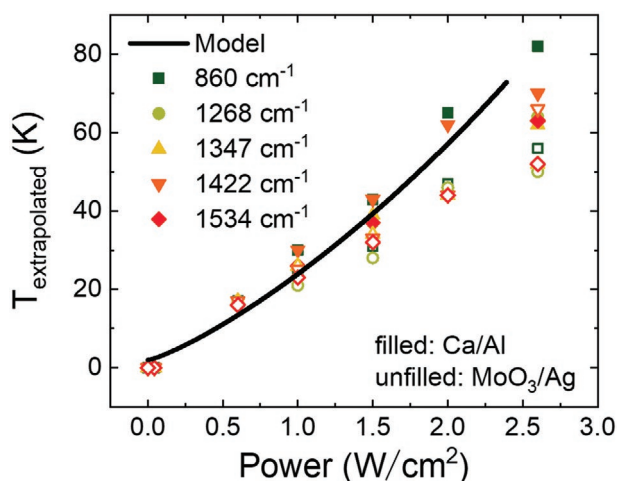


**Figure 7.** Experimental and simulated temperature values ( $T_{\text{extrapolated}}$ ) as a function of electrical power ( $P$ ) in PCPDTBT films. Closed symbols represent the diode with Ca/Al top contacts, while unfilled symbols represent diodes with MoO<sub>3</sub>/Ag top contacts; the black line represents the simulated values from the model.

self-heating in PCPDTBT diodes. The major Raman modes in the finger print region in PCPDTBT shift by up to 1.4 cm<sup>-1</sup> over a temperature range of 75 K. As the peaks are prominent and easily fit, the errors in the fits are low enough to make reliable temperature measurements. We can quantify Raman shifts as low as  $\Delta X = 0.04$  cm<sup>-1</sup>, which corresponds to a sensitivity in the temperature measurement of  $\Delta T = 4$  K. In addition to peak position, we also analyzed the behavior of the other peak parameters (width and intensity) as a function of applied bias and temperature (Figures S7 and S8, Supporting Information). We observed slight peak broadening with increasing bias and temperature, which agreed with the past reports.<sup>[66,69,70]</sup> Peak broadening revealed similar trends to the shift in the peak center, but the effect was significantly smaller, and therefore resulted in more error in the fitting (Figure S9, Supporting Information). The peak intensity did not show a discernible trend with temperature.

The impact of self-heating on the  $J$ - $V$  characteristics of the diode was confirmed by modeling, which revealed that recombination heating dominates at low to intermediate voltages (<2.5 V) while Joule heating dominates at higher voltages (>2.5 V). It should be highlighted that the temperature dependence used to model the  $J$ - $V$  characteristics is only introduced through the Fermi-Dirac distribution of the trapped and free carriers, and we neglect any dependence of the *free* carrier mobility on temperature. Thus, the results from the model represent the lower bounds of the influence of temperature on the  $J$ - $V$  curve. The complex dependence of carrier transport on electric field, temperature, and carrier density in disordered organic semiconductors prevents us from isolating the impact of self-heating alone on carrier mobility.

Previous studies have assigned shifts in the Raman spectra in donor-acceptor polymers, including PCPDTBT, to polaronic signatures due to the interaction of charge carriers with the polymer backbone resulting in either shifts in the Raman modes<sup>[72,83]</sup> or changes in mode intensity.<sup>[84]</sup> The Raman shifts observed in our experiments appear to be fully consistent with self-heating, and we could not detect any additional influences on the spectra due to vibrational Stark effects or due to polarons.

The comparison between the two device architectures (Ca/Al and MoO<sub>3</sub>/Ag) shows good agreement between the dissipated power and the extrapolated temperatures, indicating that the results reflect self-heating effects in PCPDTBT layer and are independent of the contact materials. However, heat dissipation in the device depends on several factors, including the thermal conductivity of the semiconductors and interlayers, the device architecture, and the experimental setup. Therefore, it is challenging to predict temperature increases in operational devices. Instead, our focus on simple device architecture allowed us to identify sources of self-heating and their impact on the diode  $J$ - $V$  curve.

Finally, we note that while charge carrier transport in organic semiconductors is temperature-dependent, and carrier mobility increasing with rising temperature, it is unlikely that self-heating has a positive effect on device performance. This is because self-heating is not associated with a controlled, homogeneous increase in sample temperature, but rather, with the rapid emergence of large thermal gradients across the device. Further active layer, transport layers, and contact materials

will have individual and specific contributions to self-heating, depending on their resistivity. Therefore, self-heating is more likely to lead to unreliable current-voltage characteristics that depend strongly on the specific measurement conditions, including device geometry, as well as the substrate and encapsulation materials. In some cases, self-heating may lead to a decrease in device performance due to phase change or glass transition of the active layer, interface degradation, or even destruction of the substrate and encapsulant.

In conclusion, with Raman spectroscopy we visualize self-heating in PCPDTBT diodes due to carrier transport and recombination, and demonstrate that Joule heating can have a significant impact on device performance even at moderate power densities. Our approach of monitoring the peak position of the prominent Raman peak modes in the fingerprint region is straightforward, requires no knowledge of the specific transport properties, and is therefore generally applicable to any pi-conjugated semiconductor, including small molecules and polymers. These results are relevant for device optimization and thermal management, as well as for the impact of self-heating for more fundamental studies of carrier transport in organic semiconductors.

## 4. Experimental Section

**Materials:** PCPDTBT (average Mw 7000–20 000), chlorobenzene (99.8%, Anhydrous), granular Ca (99.99%), and MoO<sub>3</sub> (99.97%) were purchased from Sigma-Aldrich and used without further purification. These materials were stored and processed in a nitrogen glove box environment. PEDOT:PSS (poly(3,4-ethylenedioxythiophene) polystyrene sulfonate) was purchased from Heraeus. Ag globules and Al wires were used as received from Umicore.

**Substrate Preparation:** ITO (Indium Tin oxide) coated glass substrates with the dimension 25 mm × 25 mm were patterned by dipping in hydrochloric acid (37% fuming) for 10 min. Next, the substrates were cleaned sequentially in acetone, isopropanol, and MiliQ water in an ultrasonic bath for 15 min in each solvent. Next, substrates were dried with a nitrogen gun, followed by UV-ozone treatment for another 15 min before further processing.

**Preparation of PCPDTBT Solution:** The polymer solution was prepared in the glove box by dissolving 20 mg mL<sup>-1</sup> PCPDTBT in anhydrous chlorobenzene. The solution was stirred at room temperature for 24 h before further use.

**PCPDTBT Diode Fabrication:** PEDOT:PSS was dissolved in isopropanol with a volume ratio 1:1. The solution was filtered using a 0.45 μm PVDF filter and then spin cast onto the cleaned glass/ITO substrates at 3500 rpm for 30 s. The PEDOT: PSS films were then thermally annealed at 393 K for 15 min on a hot plate. All processing of the PEDOT:PSS was performed in ambient atmosphere. The substrates were then transferred into a nitrogen glove box for further processing. Next, the PCPDTBT solution was spun cast at 600 rpm for 30 s to form a homogeneous film, followed by a drying step of 1000 rpm for 10 s. Part of the polymer layer was then mechanically removed to expose the ITO contact and ensure good electrical contact between the ITO and the contacting pins. Top electrodes were thermally deposited in an evaporation chamber also housed inside the glove box. Two different metal contact structures were used in this study, 1) 20 nm Ca followed by 80 nm Al and 2) 10 nm MoO<sub>3</sub> followed by 100 nm Ag. The Ca layer was used as a hole blocking layer (HBL), whereas the MoO<sub>3</sub> layer was used as a hole transporting layer (HTL).

**PCPDTBT Films on Glass:** For temperature-dependent Raman measurements, PCPDTBT solution was spin cast onto pre-cleaned glass substrates following the same cleaning procedure and deposition steps as described above. The PCPDTBT film was encapsulated before Raman measurements by applying a second glass plate to the top of the sample and sealing the structure with epoxy around the edges.

**Electrical Characterization:** The diodes were mounted inside a homemade, airtight sample holder with electrical connections. The sample holder was equipped with external electrical leads to enable measurements while keeping the sample in an inert environment. Current–Voltage measurements were performed using a Keithley 2400 source meter controlled by a LabView program.

**Coupled Electrical Raman Measurements:** Raman spectra were measured using a Renishaw inVia Raman microscope, equipped with a 532 nm laser diode and 20x magnification objective. The diodes were enclosed inside an air-tight electrical sample holder inside the N<sub>2</sub>-filled glove box and transferred for Raman measurement. The sample was placed under Raman microscope and photo-excited through the glass substrate (Figure 1a). The Raman measurement was started after the current density in the diodes reached a steady value.

**Temperature-Dependent Raman Measurements:** Encapsulated PCPDTBT/glass samples were placed on a home-built hotplate under the Raman microscope. Gradual heating and cooling of the film were done from room temperature to 373 K at steps of 10 K. The temperature of the hot plate was allowed to stabilize at each desired temperature before measurement.

**Protocol for Raman Measurements:** All Raman measurements were performed using the same protocol: A very low laser power of 4.5 μW was used to obtain three accumulations (the number of scans to produce a single spectrum) for an exposure time of 30 s (the period of time the detector is exposed to the Raman signal). Increasing the number of scans and exposure time can yield better signal-to-noise, but may degrade the sample. Therefore, the protocol was optimized for good signal-to-noise and no sample degradation. Each Raman measurement consists of a set of 10 consecutive spectra that were acquired under identical conditions according to this protocol, with a time lapse of 151 s between each spectrum. These 10 spectra were used to confirm that there are no changes in the Raman spectra due to artifacts that may arise from laser heating, sample degradation, or drift in the measurement related to laser stability or shifts in the focus spot of the microscope.

## Supporting Information

Supporting Information is available from the Wiley Online Library or from the author.

## Acknowledgements

S.M. and E.v.H. acknowledge funding by the Dutch Research Council (NWO) within the XS Program, grant number OCENW:XS.040.

## Conflict of Interest

The authors declare no conflict of interest.

## Data Availability Statement

The data that support the findings of this study are available from the corresponding author upon reasonable request.

## Keywords

conjugated polymers, organic electronics, self-heating, vibrational spectroscopy

Received: November 15, 2021

Revised: March 4, 2022

Published online:

- [1] E. K. Lee, M. Y. Lee, C. H. Park, H. R. Lee, J. H. Oh, *Adv. Mater.* **2017**, *29*, 1703638.
- [2] C. J. Brabec, A. Distler, X. Du, H. J. Egelhaaf, J. Hauch, T. Heumüller, N. Li, *Adv. Energy Mater.* **2020**, *10*, 2001864.
- [3] Y. Xu, F. Zhang, X. Feng, *Small* **2011**, *7*, 1338.
- [4] R. Ma, S. Y. Chou, Y. Xie, Q. Pei, *Chem. Soc. Rev.* **2019**, *48*, 1741.
- [5] S. E. Root, S. Savagatrup, A. D. Printz, D. Rodriguez, D. J. Lipomi, *Chem. Rev.* **2017**, *117*, 6467.
- [6] H. Sahu, W. Rao, A. Troisi, H. Ma, *Adv. Energy Mater.* **2018**, *8*, 1801032.
- [7] L. Dou, Y. Liu, Z. Hong, G. Li, Y. Yang, *Chem. Rev.* **2015**, *115*, 12633.
- [8] A. Facchetti, *Chem. Mater.* **2011**, *23*, 733.
- [9] A. Marrocchi, A. Facchetti, D. Lanari, S. Santoro, L. Vaccaro, *Chem. Sci.* **2016**, *7*, 6298.
- [10] P. Friederich, A. Fediai, S. Kaiser, M. Konrad, N. Jung, W. Wenzel, *Adv. Mater.* **2019**, *31*, 1808256.
- [11] M. O'Neill, S. M. Kelly, *Adv. Mater.* **2011**, *23*, 566.
- [12] F. Steuber, J. Staudigel, M. Stössel, J. Simmerer, A. Winnacker, H. Spreitzer, F. Weissörtel, J. Salbeck, *Adv. Mater.* **2000**, *12*, 130.
- [13] N. C. Greenham, *Nature* **1995**, *397*, 121.
- [14] R. A. J. Janssen, J. Nelson, *Adv. Mater.* **2013**, *25*, 1847.
- [15] N. Camaioni, R. Po, *J. Phys. Chem. Lett.* **2013**, *4*, 1821.
- [16] J. D. Servaites, M. A. Ratner, T. J. Marks, *Energy Environ. Sci.* **2011**, *4*, 4410.
- [17] Y. Sato, S. Ichinosawa, H. Kanai, *IEEE J. Sel. Top. Quantum Electron.* **1998**, *4*, 40.
- [18] K. Kwak, K. Cho, S. Kim, *Opt. Express* **2013**, *21*, 29558.
- [19] Q. Niu, R. Rohloff, G.-J. A. H. Wetzelaer, P. W. M. Blom, N. I. Crăciun, *Nat. Mater.* **2018**, *17*, 557.
- [20] Y. Zhang, I. D. W. Samuel, T. Wang, D. G. Lidzey, *Adv. Sci.* **2018**, *5*, 1800434.
- [21] W. R. Mateker, M. D. McGehee, *Adv. Mater.* **2017**, *29*, 1603940.
- [22] P. E. Burrows, V. Bulovic, S. R. Forrest, L. S. Sapochak, D. M. McCarty, M. E. Thompson, *Appl. Phys. Lett.* **1994**, *65*, 2922.
- [23] Z. Hu, Z. Zhong, Y. Chen, C. Sun, F. Huang, J. Peng, J. Wang, Y. Cao, *Adv. Funct. Mater.* **2016**, *26*, 129.
- [24] A. K. Y. Jen, *J. Mater. Chem.* **2010**, *20*, 2491.
- [25] R. E. Triambulo, J. W. Park, *Org. Electron.* **2016**, *28*, 123.
- [26] S. Chung, J. H. Lee, J. Jeong, J. Kim, Y. Hong, *Appl. Phys. Lett.* **2009**, *94*, 253302.
- [27] X. Zhou, J. He, L. S. Liao, M. Lu, X. M. Ding, X. Y. Hou, X. M. Zhang, X. Q. He, S. T. Lee, *Adv. Mater.* **2000**, *12*, 265.
- [28] F. A. Boroumand, A. Hammiche, G. Hill, D. G. Lidzey, *Adv. Mater.* **2004**, *16*, 252.
- [29] J. R. Gong, L. J. Wan, S. Bin Lei, C. L. Bai, X. H. Zhang, S. T. Lee, *J. Phys. Chem. B* **2005**, *109*, 1675.
- [30] I. R. De Moraes, S. Scholz, M. Hermenau, M. L. Tietze, T. Schwab, S. Hofmann, M. C. Gather, K. Leo, *Org. Electron.* **2015**, *26*, 158.
- [31] H. Nakanotani, H. Sasabe, C. Adachi, *Appl. Phys. Lett.* **2005**, *86*, 213506.
- [32] C. C. S. Chan, C. Ma, X. Zou, Z. Xing, G. Zhang, H. Yip, R. A. Taylor, Y. He, K. S. Wong, P. C. Y. Chow, *Adv. Funct. Mater.* **2021**, *31*, 2107157.
- [33] P. Tyagi, R. Srivastava, L. I. Giri, S. Tuli, C. Lee, *Synth. Met.* **2016**, *216*, 40.
- [34] L. Cui, R. Miao, K. Wang, D. Thompson, L. A. Zotti, J. C. Cuevas, E. Meyhofer, P. Reddy, *Nat. Nanotechnol.* **2018**, *13*, 122.
- [35] D. Ding, F. Sun, F. Xia, Z. Tang, *Nano Res.* **2021**, *14*, 2090.
- [36] L. Zhao, K. Roh, S. Kacmoli, K. Al Kurdi, S. Jhulki, S. Barlow, S. R. Marder, C. Gmachl, B. P. Rand, *Adv. Mater.* **2020**, *32*, 202000752.
- [37] M. W. Shin, S. H. Jang, *Org. Electron.* **2012**, *13*, 767.
- [38] J. W. Park, D. C. Shin, S. H. Park, *Semicond. Sci. Technol.* **2011**, *26*, 034002.
- [39] C. G. Zimmermann, *IEEE 40th Photovolt. Spec. Conf. PVSC* **2014**, 3612.
- [40] S. Sudheendran Swayamprabha, D. K. Dubey, Shahnawaz, R. A. K. Y., M. R. Nagar, A. Sharma, F. C. Tung, J. H. Jou, *Adv. Sci.* **2021**, *8*, 2002254.
- [41] M. M. Azrain, M. R. Mansor, G. Omar, S. H. S. M. Fadzullah, S. R. Esa, L. M. Lim, D. Sivakumar, M. N. A. Nordin, *Synth. Met.* **2019**, *247*, 191.
- [42] A. K. Jagdish, G. Pavan Kumar, P. C. Ramamurthy, D. R. Mahapatra, G. Hegde, *Org. Electron.* **2016**, *39*, 354.
- [43] J. A. McEwan, A. J. Clulow, A. Nelson, N. R. Yepuri, P. L. Burn, I. R. Gentle, *ACS Appl. Mater. Interfaces* **2017**, *9*, 14153.
- [44] S. Scholz, D. Kondakov, B. Lüssem, K. Leo, *Chem. Rev.* **2015**, *115*, 8449.
- [45] E. Knapp, B. Ruhstaller, *Proc. SPIE*, **2015**, 9566, 95660X.
- [46] H. Okumoto, T. Tsutsui, *Appl. Phys. Express* **2014**, *7*, 061601.
- [47] A. Fischer, M. Pfalz, K. Vandewal, S. Lenk, M. Liero, A. Glitzky, S. Reineke, *Phys. Rev. Appl.* **2018**, *10*, 014023.
- [48] A. Fischer, T. Koprucki, K. Gärtner, M. L. Tietze, J. Brückner, B. Lüssem, K. Leo, A. Glitzky, R. Scholz, *Adv. Funct. Mater.* **2014**, *24*, 3367.
- [49] M. P. Klinger, A. Fischer, H. Kleemann, K. Leo, *Sci. Rep.* **2018**, *8*, 9806.
- [50] A. Kirch, A. Fischer, M. Liero, J. Fuhrmann, A. Glitzky, S. Reineke, *Light: Sci. Appl.* **2020**, *9*, 2047.
- [51] A. Fischer, P. Pahnner, B. Lüssem, K. Leo, R. Scholz, T. Koprucki, J. Fuhrmann, K. Gärtner, A. Glitzky, *Org. Electron.* **2012**, *13*, 2461.
- [52] X. A. Cao, X. M. Li, R. Y. Yang, Y. M. Zhou, *IEEE Electron Device Lett.* **2015**, *36*, 847.
- [53] K. Yoshida, T. Matsushima, H. Nakanotani, C. Adachi, *Org. Electron.* **2016**, *31*, 191.
- [54] K. Yoshida, H. Nakanotani, C. Adachi, *Org. Electron.* **2016**, *31*, 287.
- [55] P. W. M. Blom, M. J. M. De Jong, M. G. Van Munster, *Phys. Rev. B* **1997**, *55*, R656.
- [56] F. So, D. Kondakov, *Adv. Mater.* **2010**, *22*, 3762.
- [57] R. P. Fornari, P. W. M. Blom, A. Troisi, *Phys. Rev. Lett.* **2017**, *118*, 086601.
- [58] S. Fratini, M. Nikolka, A. Salleo, G. Schweicher, H. Sirringhaus, *Nat. Mater.* **2020**, *19*, 491.
- [59] C. Gärditz, A. Winnacker, F. Schindler, R. Paetzold, *Appl. Phys. Lett.* **2007**, *90*, 103506.
- [60] H. Tsuji, Y. Furukawa, *Chem. Phys. Lett.* **2010**, *488*, 206.
- [61] T. Sugiyama, H. Tsuji, Y. Furukawa, *Chem. Phys. Lett.* **2008**, *453*, 238.
- [62] S. Xu, A. Fan, H. Wang, X. Zhang, X. Wang, *Int. J. Heat Mass Transfer* **2020**, *154*, 119751.
- [63] E. Alarcón-Lladó, S. Bin-Dolmanan, V. K. X. Lin, S. L. Teo, A. Dadgar, A. Krost, S. Tripathy, *J. Appl. Phys.* **2010**, *108*, 114501.
- [64] S. Sandell, E. Chávez-Ángel, A. El Sachat, J. He, C. M. Sotomayor Torres, J. Maire, *J. Appl. Phys.* **2020**, *128*, 131101.
- [65] R. A. Cowley, *J. Phys.* **1965**, *26*, 659.
- [66] G. Lucazeau, *J. Raman Spectrosc.* **2003**, *34*, 478.
- [67] R. Tsu, J. G. Hernandez, *Appl. Phys. Lett.* **1982**, *41*, 1016.
- [68] M. Balkanski, R. F. Wallis, E. Haro, *Phys. Rev. B* **1983**, *28*, 1928.
- [69] A. Compaan, H. J. Trodahl, *Phys. Rev. B* **1984**, *29*, 793.
- [70] S. Wood, J. R. Hollis, J. S. Kim, *J. Phys. D: Appl. Phys.* **2017**, *50*, 073001.
- [71] S. Kouteva-Arguirova, T. Arguirov, D. Wolfframm, J. Reif, *J. Appl. Phys.* **2003**, *94*, 4946.
- [72] E. J. J. Martin, N. Bérubé, F. Provencher, M. Côté, C. Silva, S. K. Doorn, J. K. Grey, *J. Mater. Chem. C* **2015**, *3*, 6058.
- [73] F. Provencher, N. Bérubé, A. W. Parker, G. M. Greetham, M. Towrie, C. Hellmann, M. Côté, N. Stingelin, C. Silva, S. C. Hayes, *Nat. Commun.* **2014**, *5*, 4288.
- [74] F. Aziz, Z. Ahmad, M. A. Najeeb, H. A. Malik, S. M. Abdullah, F. Touati, K. Sulaiman, *Appl. Phys. A: Mater. Sci. Process.* **2017**, *123*, 773.
- [75] G. U. Bublitz, S. G. Boxer, *Annu. Rev. Phys. Chem.* **1997**, *48*, 213.
- [76] Z. Qian, Z. Cao, L. Galuska, S. Zhang, J. Xu, X. Gu, *Macromol. Chem. Phys.* **2019**, *220*, 201900062.



- [77] General-purpose photovoltaic model, [www.gpvdm.com](http://www.gpvdm.com) (accessed: November 2021).
- [78] R. C. I. MacKenzie, C. G. Shuttle, M. L. Chabiny, J. Nelson, *Adv. Energy Mater.* **2012**, *2*, 662.
- [79] J. A. Röhr, R. C. I. Mackenzie, *J. Appl. Phys.* **2020**, *128*, 165701.
- [80] N. Majeed, M. Saladina, M. Krompiec, S. Greedy, C. Deibel, R. C. I. MacKenzie, *Adv. Funct. Mater.* **2020**, *30*, 201907259.
- [81] E. M. Azoff, *Solid State Electron.* **1987**, *30*, 913.
- [82] E. M. Azoff, *Ph.D. Thesis*, Rutherford Appleton Laboratory, UK **1986**.
- [83] F. Deschler, D. Riedel, A. Deák, B. Ecker, E. Von Hauff, E. Da Como, *Synth. Met.* **2015**, *199*, 381.
- [84] C. Francis, D. Fazzi, S. B. Grimm, F. Paulus, S. Beck, S. Hillebrandt, A. Pucci, J. Zaumseil, *J. Mater. Chem. C* **2017**, *5*, 6176.